



HAL
open science

Retrieval of Monsoon Landslide Timings With Sentinel-1 Reveals the Effects of Earthquakes and Extreme Rainfall

K. Burrows, O. Marc, Christoff Andermann

► To cite this version:

K. Burrows, O. Marc, Christoff Andermann. Retrieval of Monsoon Landslide Timings With Sentinel-1 Reveals the Effects of Earthquakes and Extreme Rainfall. *Geophysical Research Letters*, 2023, 50 (16), pp.e2023GL104720. 10.1029/2023GL104720 . hal-04187861

HAL Id: hal-04187861

<https://hal.science/hal-04187861v1>

Submitted on 29 Aug 2023

HAL is a multi-disciplinary open access archive for the deposit and dissemination of scientific research documents, whether they are published or not. The documents may come from teaching and research institutions in France or abroad, or from public or private research centers.

L'archive ouverte pluridisciplinaire **HAL**, est destinée au dépôt et à la diffusion de documents scientifiques de niveau recherche, publiés ou non, émanant des établissements d'enseignement et de recherche français ou étrangers, des laboratoires publics ou privés.



Distributed under a Creative Commons Attribution 4.0 International License

Geophysical Research Letters®



RESEARCH LETTER

10.1029/2023GL104720

Retrieval of Monsoon Landslide Timings With Sentinel-1 Reveals the Effects of Earthquakes and Extreme Rainfall

K. Burrows^{1,2} , O. Marc¹ , and C. Andermann^{3,4} 

¹University of Toulouse Paul Sabatier, Géosciences Environnement Toulouse (GET), UMR, CNRS/IRD/CNES/UPS, Observatoire Midi-Pyrénées, Toulouse, France, ²European Space Agency (ESA-ESRIN) Science Hub, Frascati, Italy, ³Géosciences Rennes, University Rennes, CNRS, UMR, Rennes, France, ⁴Helmholtz Centre Potsdam, GFZ German Research Center for Geosciences, Section 4.6: Geomorphology, Potsdam, Germany

Key Points:

- We use Sentinel-1 time series to constrain the timings of hundreds of monsoon-triggered landslides across Nepal in 2015, 2017, 2018, and 2019
- We identify spatio-temporal clusters of landslides and associate them with particular periods of intense rainfall
- We use landslide timing information to calibrate numerical models of soil saturation and infer post-seismic hillslope weakening in 2015

Supporting Information:

Supporting Information may be found in the online version of this article.

Correspondence to:

K. Burrows,
katy.burrows@esa.int

Citation:

Burrows, K., Marc, O., & Andermann, C. (2023). Retrieval of monsoon landslide timings with Sentinel-1 reveals the effects of earthquakes and extreme rainfall. *Geophysical Research Letters*, 50, e2023GL104720. <https://doi.org/10.1029/2023GL104720>

Received 26 MAY 2023

Accepted 13 AUG 2023

Abstract Monsoon rainfall triggers hundreds of landslides across Nepal every year, causing significant hazard and mass wasting. Annual inventories of these landslides have been mapped using multi-spectral satellite images, but these images are obscured by cloud cover during the monsoon, making it impossible to use them to constrain landslide timing. We employ recently developed techniques to derive individual timings from Sentinel-1 for 579 landslides in 2015, 2017, 2018, and 2019 in Nepal. We use this new timing information alongside satellite rainfall data to identify spatio-temporal clusters of landslides and associate these with periods of particularly intense rainfall. We also observed that during the 2015 monsoon, many landslides failed earlier and in dryer conditions than in 2017–2019. We use physical models to demonstrate how this requires a temporary loss of hillslope strength following the M_w 7.8 Gorkha Earthquake sequence and suggest a modeled cohesion loss in the range 1–3 kPa.

Plain Language Summary Earthquakes, storms and long periods of rain during the monsoon all contribute to landsliding in Nepal. Understanding these different triggers requires information on where and when landslides happen every year. We applied a new landslide timing method based on Sentinel-1 satellite images alongside satellite measurements of rainfall to model the amount of rain needed to trigger individual landslides during the monsoon. This allowed us to connect landslides with particular storms and to observe the influence of a large earthquake in 2015 on landslide timing. Landslides occurred in unusually dry conditions following the earthquake, which can be interpreted as a temporary weakening of the landscape.

1. Introduction

Worldwide, landsliding is frequently caused by intense rainfall (Guzzetti et al., 2008; Marc et al., 2018), leading to hundreds of casualties every year (Petley et al., 2007). In the Himalayas, hundreds of landslides are triggered annually by heavy rainfall between May and October, damaging vital infrastructure and posing a significant hazard to communities. In addition to rainfall, widespread landsliding can also result from earthquakes. Recently, the 2015 M_w 7.8 Gorkha earthquake in Nepal triggered over 25,000 landslides and resulted in elevated levels of landsliding during subsequent monsoon seasons (Jones et al., 2021; Marc et al., 2019; Roback et al., 2018). Sustained cloud cover, which often lasts months during the monsoon, obscures commonly used satellite observation products and has limited previous analyses to multi-annual inventories (Jones et al., 2021; Kinsey et al., 2021; Marc et al., 2019). This lack of landslide timing information within the monsoon period limits our understanding of landslide triggering, which is thought to depend on both hydrological recharge by the monsoon (Gabet et al., 2004; Illien et al., 2021), intense bursts of rainfall (Jones et al., 2021), and post-seismic regolith disturbance (Marc et al., 2019, 2021). Characterization of a large number of landslides in terms of both location and timing is crucial to untangle the influence of these multiple triggering mechanisms, and ultimately improve physical and empirical models of landslide hazard.

In some cases, information on landslide timing can be obtained through interviews with local residents and news reports (Bell et al., 2021) or through analysis of signals recorded by seismic networks (Hibert et al., 2019). However, these methods are often limited to large landslides (for seismic methods) and those in populated areas (for reports and interviews). In contrast, Synthetic Aperture Radar (SAR) satellite data may offer a more generally applicable landslide timing technique. SAR images can penetrate cloud and are sensitive to changes in surface roughness and vegetation cover caused by landslides (Mondini et al., 2021). Recently, methods have

© 2023 The Authors.

This is an open access article under the terms of the [Creative Commons Attribution-NonCommercial License](https://creativecommons.org/licenses/by/4.0/), which permits use, distribution and reproduction in any medium, provided the original work is properly cited and is not used for commercial purposes.

been developed that use Sentinel-1 time series to constrain landslide timings with a resolution of up to 12 days (Burrows et al., 2022; Deijns et al., 2022). Although 12 days is less precise than previous methods, it is sufficient to better understand complex triggering, and these new methods greatly increase the potential spatial scope of studies requiring landslide timing.

Here, we demonstrate the novel capability of Sentinel-1 time series to constrain the timings of hundreds of mapped landslide polygons triggered during four monsoon seasons following the Gorkha earthquake in Nepal (2015 and 2017–2019). Using this timing information alongside calibrated satellite rainfall products, we identify spatio-temporal clusters of landslides and relate these to specific periods of intense rainfall within the monsoon, offering new insights on hydro-meteorological thresholds (Bogaard & Greco, 2018) and the role of extreme rainfall (Jones et al., 2021). We also use physical models to estimate the soil water saturation when each landslide failed, which can then be used to infer hillslope strength parameters. The large numbers of landslides considered in the study allow us to infer bulk changes in hillslope strength between years. Thus, landslide timing information offers a new way to study the transient post-seismic weakening that has been observed following large earthquakes (Brain et al., 2021; Jones et al., 2021; Marc et al., 2015, 2019).

2. Materials and Methods

We apply a two-step process in which landslides are first mapped as polygons using multi-spectral satellite images and then constrained in time using Sentinel-1 time series. This timing information allows us to model the soil saturation at the time of failure from satellite rainfall products, which can then be used in a simple hillslope stability model (Figure S1 in Supporting Information S1).

2.1. Landslide Timings From Sentinel-1

Here we use the landslide timing method of Burrows et al. (2022) since it allows individual landslides in an inventory to be assigned different timings and we do not expect monsoon-triggered landslides to occur simultaneously. This method, which allows 30% of the landslides in an inventory to be timed with an accuracy of 80%, is summarized in Figure S1 in Supporting Information S1 and detailed in Burrows et al. (2022).

The method requires a simultaneous step change in at least two of four metrics calculated for each polygon from the γ_0 backscatter derived from Sentinel-1 ground range detected (GRD) image time series in Google Earth Engine:

- Average amplitude compared to the local background amplitude
- Variability between pixels
- Geometric shadows
- Geometric bright spots (dihedral scattering)

In most cases, the precision of the timing is the same as the Sentinel-1 repeat time: 12 days. In a small number of cases, this increases to 24 or 36 days due to missing Sentinel-1 acquisitions or is decreased when a landslide is timed by both the ascending and descending satellite orbits.

2.2. Landslide Data Compilation

We applied the techniques from Section 2.1 to four annual inventories of monsoon-triggered landslides between 2015 and 2019. First, three compiled over central and eastern Nepal by Jones et al. (2021) for 2015, 2017 and 2018. 2016 was omitted due to poor Sentinel-1 coverage over Nepal during that monsoon season. For the same reason, the landslide timing methods could not be applied to the central-southern part of the 2015 inventory. We also prepared an additional inventory for the 2019 monsoon season over the same area mapped by Jones et al. (2021) and extended each inventory further west (Figure 1a). All inventories were prepared through comparison of pan-sharpened Landsat 8 images acquired before and after each monsoon season. We discarded polygons under 2000 m², since this is the minimum size at which Burrows et al. (2022) tested their methods and since inventories compiled from medium resolution imagery such as Landsat 8 may be incomplete for small events. This left 3,373 landslides across the four monsoon seasons (Figure 1a), of which we were able to constrain the timings of 579 events.

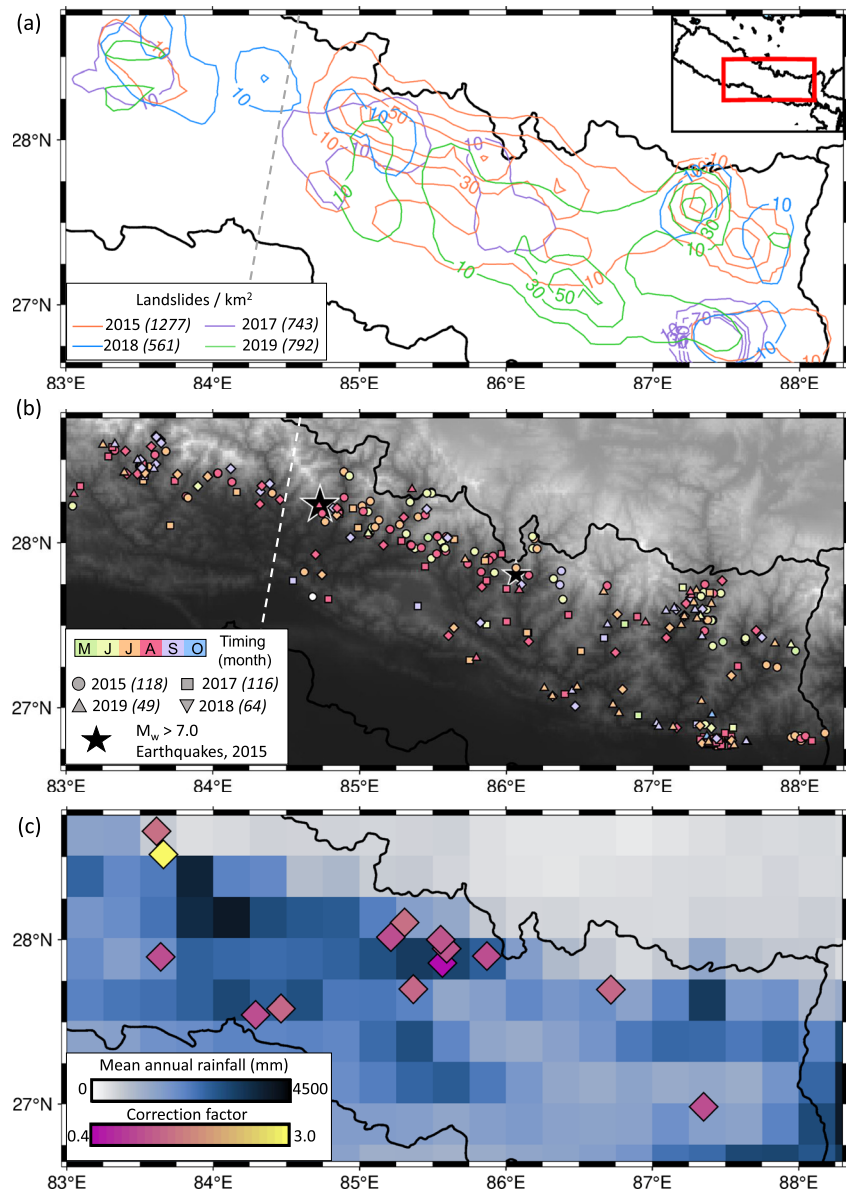


Figure 1. (a) Density of landslides $>2,000 \text{ m}^2$ per km^2 from the inventories of Jones et al. (2021) and this study. Dashed line shows western limit of the area mapped by Jones et al. (2021). The number of landslides in each year is given in brackets. (b) Locations of landslides with timings constrained using Sentinel-1. Points are colored by the month in which the midpoint of the Sentinel-1 time window lies. (c) Average total monsoon rainfall based on gauge-corrected GPM. Markers show gauge locations.

To assess whether there were bulk differences in landslide properties between years that could influence their timings and to constrain the hillslope stability model, we characterized all landslide scars by their area, A_s , median slope, θ_s , 90th percentile drainage area, Dr_{90} , and thickness, T_s . A_s was estimated from the area and perimeter of each landslide polygon according to the formulas presented in Marc et al. (2018). θ_s and Dr_{90} were derived from the shuttle radar topography mission (SRTM-30m) digital elevation model (DEM) in QGIS (Farr et al., 2007). T_s was estimated from A_s according to the empirical relationships of Larsen et al. (2010).

We removed 197 landslides with high drainage areas ($>10^{4.5} \text{ m}^2$) that could have been influenced by lateral rather than vertical infiltration (Iverson, 2000). We also examined each timed landslide in high resolution satellite images in Google Earth Explorer and excluded 16 polygons that appeared not to be landslides, but instead features relating to human activity (e.g., construction or agriculture) and 23 landslides that were likely to have

been influenced by factors other than rainfall, leaving 347 landslides (Figure 1b). These 23 included: 17 landslides that intersected roads, which are often poorly engineered and can bring slopes closer to failure (Pradhan et al., 2022); 5 bank collapses next to rivers, whose timing is likely determined by river flooding or undercutting; and finally a large rockslide that dammed the Kali Gandaki River in 2015 but that field observations suggest was a delayed earthquake-triggered landslide (Collins & Jibson, 2015).

2.3. Rainfall Data Sets and Calibration

In order to model soil saturation through time for each landslide, we used the NASA GPM IMERG satellite rainfall product, which combines microwave and infrared measurements from a constellation of satellites (Huffman et al., 2015). This product offers continuous rainfall estimates, covers the whole spatial extent and duration of our study, and captures the spatial distribution of annual precipitation and the frequency of wet days over Nepal well (Talchabhadel et al., 2022). However, it generally underestimates rainfall during the monsoon when compared to rain gauges and struggles to capture orographically induced precipitation, leading it to underestimate precipitation at high altitudes in Nepal (Sharma et al., 2020).

To address these shortcomings, we calibrated the GPM rainfall, R , using gauge data in two steps. In each step, we derive a corrected rainfall $R_{corr} = aR^b$, by optimizing a and b to minimize the difference in cumulative distribution function (CDF) between R_{corr} and the calibration rainfall. Both CDFs only take rainy days (>0.05 mm of rain in both data sets) during the monsoon (15 April–15 October).

First, we used the APHRODITE rainfall product (Yatagai et al., 2012). For Nepal, APHRODITE ends in 2015, and so does not cover the period required for this study, but it is based on rain gauge data so its spatial pattern should better recreate the orographic effect than GPM. As a gridded product derived from gauge data across the country, it also provides more complete spatial coverage than individual gauges. We took the GPM and APHRODITE data sets from 2010 to 2015 and downsampled the GPM data onto the 0.25° grid of the APHRODITE data set. Thus, a and b were constrained at each pixel (Figure S2 in Supporting Information S1), and corrected GPM rainfall was derived for the study period, 2015–2019.

Second, we repeated the calibration procedure on the APHRODITE-corrected GPM, using individual rain gauges (Table S1 in Supporting Information S1, Figure 1c). Here, most pixels display $a \sim 1$ and $b > 1$ meaning that the APHRODITE-corrected GPM underestimated the rainfall recorded by the gauges, especially at high magnitude values, probably because the APHRODITE product represents the mean rainfall over a large pixel (0.25°). This underestimation appears worse at high elevations, probably due to the relatively sparse network of gauges in the High Himalayas that were used to derive APHRODITE. In order to better estimate the monsoon-rainfall, we apply a further correction across the whole study area, using median values of a and b , 1.11 ± 0.54 and 1.18 ± 0.13 , respectively (Figure 1c).

2.4. Soil Moisture Model

To model at first order the shallow regolith hydrology, we used a “leaky bucket” approach (Gabet et al., 2004; Wilson & Wiczorek, 1995), in which the evolution through time of the soil water content W_t is dominated by local rainfall input R_t minus evapotranspiration, E . This process is estimated using Equation 1 until the field capacity FC is reached.

$$W_t = W_{t-1} + (R_t - E) \quad (1)$$

FC is determined from the porosity η , drained porosity η_d and regolith thickness h_s . h_s was obtained from the depths estimated in Section 2.2. We took constant values of $\eta = 0.4$ and $\eta_d = 0.15$ following Gabet et al. (2004).

$$FC = h_s(\eta - \eta_d) \quad (2)$$

Once W_t exceeds FC , water begins to drain from the system and its evolution is described by Equation 3:

$$W_t = W_{t-1}e^{-k} + \left(\frac{R_t(1 - e^{-k})}{k} - E \right) \quad (3)$$

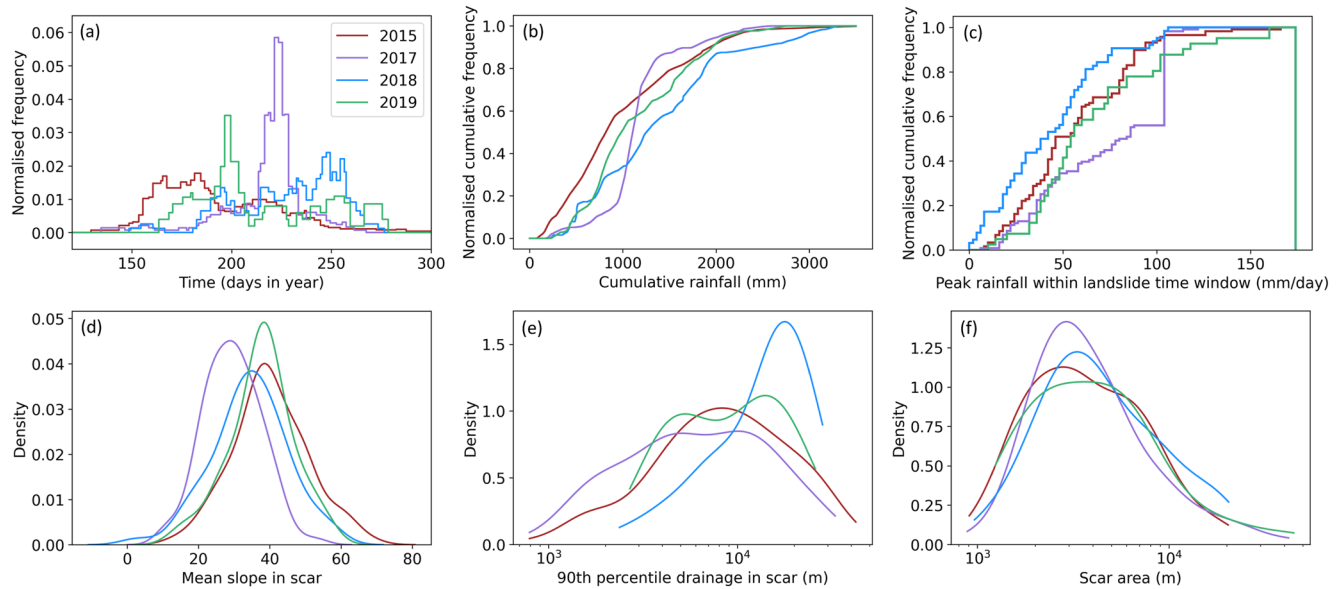


Figure 2. Characteristics of timed landslides: (a) timing (b) Cumulative rainfall from 15th April to landslide timing (c) peak daily rainfall within time window (d) kernel density of slope gradient in scar (e) kernel density of 90th percentile drainage area for pixels within scar (f) scar area kernel density.

with k a non-dimensional drainage parameter. The system is allowed to vary between dry ($W = 0$) and saturated ($W = h_w$). We used values of $E = 3$ mm/day (appropriate for Nepal given the season and elevation range of the study (Lambert & Chitrakar, 1989)) and $k = 0.02$.

With the landslide timing information obtained using the methods from Section 2.1, we can use W at the time of failure in the Factor of Safety equation (FoS).

$$FoS = \frac{\tan(\phi)}{\tan(\theta)} + \frac{C - gh_w \rho_w \tan(\phi)}{gh_s \rho_s \sin(\theta) \cos(\theta)} \quad (4)$$

At the point of failure, $FoS = 1$, h_w , the vertical water height was obtained by taking the maximum value of W within the landslide timing window and reprojecting it into the vertical plane. Thus, using standard values for the density of the water and soil, $\rho_w = 1,000$ kg/m³ and $\rho_s = 2,600$ kg/m³ respectively, we are left with two unknowns: cohesion, C , and internal friction angle, ϕ . Assuming $\phi = \theta$ we can retrieve C (in kPa) for each timed landslide. Alternative scenarios are discussed in Section 4.1.

3. Results

3.1. Landslide Characteristics

The distribution of landslide timings varies noticeably between years (Figure 2a). In addition to distributed timings between mid-June and mid-September, most years contain temporal clusters. Sharp peaks are seen in August 2017 and July 2019 that align with widely reported flood events (Government of Nepal, 2017; Government of Nepal, 2019), while 2015 and 2018 show concentration of landsliding in early June and September, respectively. In terms of rainfall (Figures 2b and 2c), the clustered nature of 2017 landsliding is striking with nearly half of the timed landslides occurring with moderate cumulative rainfall $R_c \sim 1,000$ mm but intense peak daily rainfall of $I_d \sim 100$ mm/day. 2019 landslides have distributed peak and cumulative rainfall, while in 2015 about 60% of the landslides occurred with $R_c < 1,000$ mm, and in 2018 landslides occurred at comparatively low I_d and high R_c .

Distributions of A_s and Dr_{90} for our timed landslides are similar between years, except for 2018 which has generally higher drainage areas (Figure 2). Slope gradient is more variable and landslides triggered in 2015 generally occurred on somewhat steeper slopes than in other years.

3.2. Modeling Regolith Saturation and Strength at Failure

The soil saturations at failure S_{fail} modeled with Equations 1–3 span the range 0–1 and tend to decrease with slope gradient (Figure 3a). In 2017, 2018 and 2019, 82% of the timed landslides were triggered with $S_{fail} > FC$, while

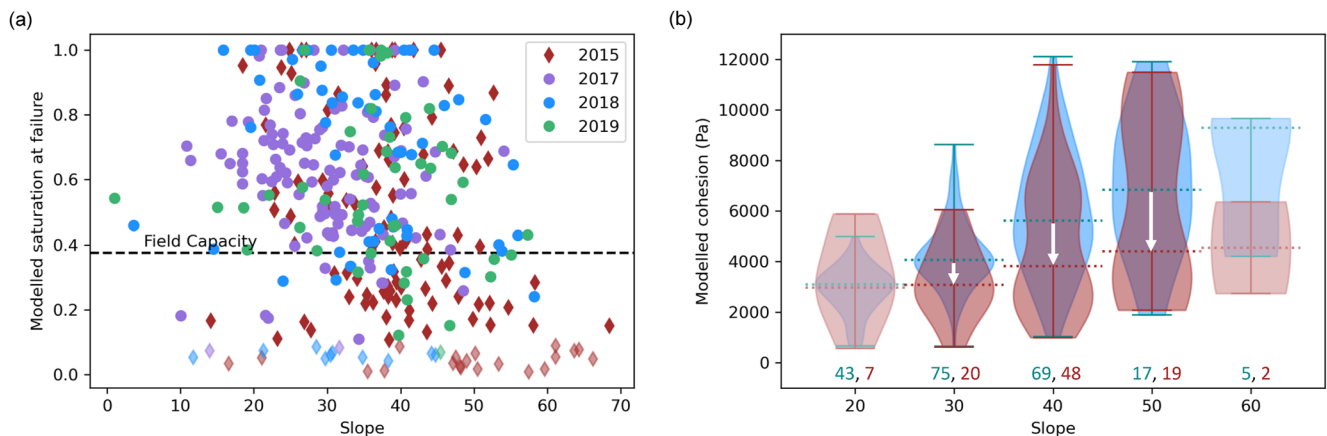


Figure 3. (a) The maximum modeled soil saturation within the 12-day Sentinel-1 time window for each landslide based on a leaky bucket model. Landslides with $S_{\text{fail}} < 0.1$ are faded out (b) Modeled cohesion based on soil moisture values from (a) for 2015 (red) and 2017–2019 (blue). The number of landslides in each violin is given at the bottom of the plot. Dashed lines show medians with white arrows showing the median cohesion drop in 2015 compared to other years. Ranges 15–25 and 55–65 are faded out since they contain insufficient (<10) landslides.

this proportion was only about 50% in 2015 (Figure 3a). From these lower saturation levels, we retrieve lower cohesion values for the 2015 landslides when binning by slope gradient (Figure 3b). 33 Landslides with $S_{\text{fail}} < 0.1$ are excluded from this modeling, since they are assumed to be either incorrectly timed by Sentinel-1, triggered by rainfall underestimated by GPM (Section 4.2) or triggered by a mechanism other than vertical infiltration (Section 4.3). Difference in median cohesion between 2015 and other years increases from around 1 kPa at a slope of 30° to closer to 3 kPa at a slope of 50°.

4. Discussion

We obtained landslide timing information for 374 landslides triggered during the 2015, 2017, 2018, and 2019 monsoon seasons. While the method described in Section 2.1 is only 80% accurate, if 1/5 of our landslide timings are incorrect, our two main results remain valid: first, the identification of spatio-temporal clusters of landslides related to specific periods of intense rainfall for example, August 2017, and second, that the 2015 monsoon resulted in earlier and drier landslides compared to other years, which could be interpreted as lower cohesion (2a,2c and 3). However, this 80% accuracy, along with the 12-day timing precision and uncertainties in our rainfall product and in parameters such as regolith depth, prevents us from deriving local hydro-meteorological thresholds (Dahal & Hasegawa, 2008) or establishing minimum values of daily and cumulative rainfall for landslide triggering (Gabet et al., 2004) (Figure S3 in Supporting Information S1).

4.1. Sensitivity to Under-Constrained Model Parameters

Various modeling parameters (E , h_s , η , η_d , and k) may vary spatially and would ideally be constrained by field-work, but this is impractical for a study carried out on this spatial scale. Instead, we consider that, while individual landslides may be imperfectly modeled, when we apply these models to large numbers of landslides (occurring in different years but in the same landscape and with similar characteristics (Figures 2d–2f)), the effects of errors in these modeling parameters should be similar across years so that the difference observed between 2015 and later years remains valid.

This assumes that these parameters are static in time. However, a temporary increase in permeability has been observed following earthquakes (Illien et al., 2022; Wang & Chia, 2008). By using the same value of k for all years rather than allowing water to drain faster in 2015 due to enhanced permeability, we may have overestimated S_{fail} in 2015 relative to other years. We also explored a scenario in which k is correlated with slope, which also resulted to an increased difference in modeled cohesion in 2015 (generally steeper slopes than other years). Our modeled difference in S_{fail} and cohesion is therefore a conservative estimate.

ϕ is also poorly constrained, but assigning it a fixed value (25°–45°) gives inconsistent results, requiring either negative or unrealistically high cohesion values (Figure S4 in Supporting Information S1). Instead, with $\phi = \theta$

in the range 30° – 50° , we obtain cohesions between 2 and 10 kPa, values that are typical for shallow landslides (Gabet et al., 2004; von Ruetten et al., 2014; Wu & Sidle, 1995). This is consistent with recent studies where landslide susceptibility (whether triggered by rainfall or earthquakes) was found to scale with slope normalized by the landscape median rather than absolute slope, suggesting that mechanical strength (i.e., ϕ) is adjusted to the landscape (i.e., θ) (Emberson et al., 2021; Marc et al., 2018; Milledge et al., 2019). Furthermore, fixing $C = 4,000$ kPa in Equation 4 and solving for ϕ yields a strong correlation between ϕ and θ and a reduced ϕ value in 2015 (Figures S4 and S5 in Supporting Information S1).

4.2. Spatio-Temporal Clusters of Landslides and the Role of Intense Rainfall

Landslide timings were not evenly distributed through time (Figure 2a) but instead can be related to short periods of intense rainfall that triggered spatio-temporal clusters of landslides. This is significant since it has previously been suggested that monsoon season containing an extreme rainfall event have much higher levels of mass-wasting than would be expected based on overall levels of monsoon rainfall (Jones et al., 2021). Establishing individual landslide timing as we have done will allow us to better compare the relative importance of continuous monsoon rainfall and intense rainfall bursts in terms of landslide erosion and hazard.

The largest spatio-temporal cluster of landslides we identify is associated with heavy rains in the Terai region from 11–14 August 2017 (Government of Nepal, 2017) and is clearly visible in Figure 2a. Recalling that our method retrieves timings for 30% of the landslides with 80% accuracy, a spatio-temporal cluster should contain around a quarter (0.3×0.8) of the landslides in a given spatial cluster. 66 of the 116 landslides for which we have timing information in 2017 overlap with this event, with 59 of these lying within an area <150 km² in eastern Terai. This sector represents 0.3% of the area mapped by Jones et al. (2021) but contains 41% of the 2017 landslides. This demonstrates the significant impact of a short localized rainfall event in terms of overall landslide numbers in 2017, even though Jones et al. (2021) did not identify 2017 as an outlier when investigating how mass wasting scales with overall monsoon intensity.

In 2018, a spatial cluster is visible in the Kali Gandaki Valley (Figure 1a), with 40 landslides located in an area <40 km². However, when we apply our timing methods in this location, we can divide it into two spatio-temporal clusters, with 4 timed landslides in early-mid August and 4 in mid September. Bell et al. (2021) have suggested several factors that could explain the high levels of landslide activity in the Kali Gandaki during this monsoon season, including an extreme rainfall event on the 13th of September that was recorded by rain gauge and melting snow during August. Bell et al. (2021) noted that neither of these events was captured by GPM, consistent with our GPM-based modeling, where both clusters have $S_{\text{fail}} < 0.1$, plotting at the bottom of Figure 3a.

We observed 13 landslides that occurred early during the 2015 monsoon season in the adjacent Sankhuwasabha and Taplejung Districts in north-eastern Nepal. This spatio-temporal cluster, occurring at a time when the cumulative rainfall in the regolith would be very low, is most likely associated with very heavy rain and flooding reported on the 10th and 11th of June in this location (Floodlist, 2015). 11 of the landslides were assigned time windows overlapping with this rainfall event, which seems underestimated in GPM, possibly due to its small spatio-temporal scale. Landslides in July 2019 can also be correlated with reports of heavy rainfall from the 11–12 of that month (Government of Nepal, 2019). One cluster of 3 timed landslides overlapping with this event was observed in Sankhuwasabha district as well as a more spatially dispersed group of 8 landslides across the eastern Terai region. Finally, we assigned timings to two landslides belonging to a tight spatial cluster of 9 in Ramechhap district, linking them with a 4-hr intense rainfall event reported there on 15 July 2017 (Gautam & Dong, 2018).

Overall, short periods of intense rainfall appear to influence overall landslide numbers, particularly in 2017. This has implications for future landslide hazard under climate change, which is expected to make intense rainfall events more likely (Kirschbaum et al., 2020).

4.3. New Constraints on Post-Seismic Landscape Disturbance

The constraints on landslide timing we have obtained here represent a new opportunity to quantify and understand the landscape disturbance caused by earthquakes. We observed landslides occurring earlier and in response to less rainfall in 2015 than in other years (Figures 2a–2c). Increased susceptibility to rainfall-triggered landsliding

within earthquake-affected areas has been observed for several events with a return to normal conditions within 1 to a few years (Jones et al., 2021; Marc et al., 2015, 2019). It has been suggested that elevated landslide rates could be the result of weakened regolith or of enhanced rainfall infiltration, supported by observations of widespread co-seismic ground cracking (Collins & Jibson, 2015; Owen et al., 2008). Transient changes, sometimes with similar temporal dynamics, have also been observed in geophysical metrics such as shallow seismic velocity or rock permeability (Illien et al., 2022; Marc et al., 2021).

Hillslope stability models indicate a cohesion loss of between 1 and 3 kPa for 2015 landslides and a large increase in the proportion of weak (<3 kPa) landslides (Figure 3b), or an equivalent weakening in terms of friction (Figure S5 in Supporting Information S1). In exploring the effect of earthquake shaking on brittle rocks, Brain et al. (2021) revealed a complicated response in terms of both cohesion and friction that is both path-dependent and varies depending on the intensity of ground shaking experienced. Thus the true process may be a combined loss of friction and cohesion.

Most co-seismic landslides occurred at longitudes between 84.5 and 86.5 (Roback et al., 2018) and the area across which higher landslide frequencies were observed, while larger, does not extend as far as the Kali Gandaki Valley (Marc et al., 2019). However, we observed the same shift in landslide timing in the west of our study area as elsewhere. 7/15 (47%) of the 2015 landslides west of the dashed line in Figure 1 occurred before the field capacity was reached compared to 52/103 (50%) east of this line and 41/229 (18%) in 2017, 2018 and 2019 combined. The spatial extent of the weakened area, as revealed by early landslides, is therefore larger than the area impacted by co-seismic landslides as well as the area across which higher landslide frequency is observed.

Twenty landslides in 2015 (17% compared to 3% in 2017–2019) occurred in May–June and in very dry conditions ($S_{\text{fail}} < 0.1$). Landslides are generally less likely this early in the monsoon, particularly before the field capacity of the regolith is reached (Gabet et al., 2004; Illien et al., 2021). It is possible that these 20 may be better explained by an alternative failure mechanism. 18 were located in the area which underwent the strongest shaking during the earthquake and experienced the most aftershocks. With the exception of one whose timing aligns with the M_w 7.3 Dolakha aftershock on the 12th May, these landslides occurred too late to have been directly triggered by aftershocks. Beyond undetected rainfall or incorrect timing, these landslides may be explained by progressive failure following the earthquake, as was suggested for the Baisari rockslide (Collins & Jibson, 2015).

5. Conclusions

We used Sentinel-1 to constrain the timings of 579 landslides triggered during the 2015, 2017, 2018, and 2019 monsoon seasons in Nepal. Using these data alongside satellite rainfall data, we were able to obtain two main results. First, we identified spatio-temporal clusters of landslides associated with specific intense rainfall events. In one case, we found that up to 40% of the landslides in an annual inventory were associated with a single intense rainfall event, highlighting the need for further research into the relative importance of long duration rainfall and shorter, more intense rainfall in determining the mass wasting effect of the Nepal monsoon. Second, when comparing the bulk properties of landslides between years, we observed comparatively early landsliding during the 2015 monsoon following the M_w 7.8 Gorkha earthquake. Numerical modeling of soil water content through time suggests that these landslides occurred in unusually dry conditions, requiring either a change in triggering mechanism or a weakened hillslope in 2015 compared to other monsoon years.

Unimpeded by cloud cover, Sentinel-1 resolves landslide timing much better than previous approaches based on optical imagery. Beyond Nepal and monsoon-affected areas, the method could be applied to any landslide inventory in vegetated environments whose timings are poorly constrained and thus difficult to assign to a specific trigger, for example, landslides triggered during sequences of storms or earthquakes, including post-seismic rainfall-triggered landsliding (Amatya et al., 2023; Ferrario, 2019; Jones et al., 2023). Our study thus highlights the value that Sentinel-1 could have in disentangling the effects of multiple landslide-triggering events in cloudy conditions.

Data Availability Statement

Landslide polygons for 2015, 2017 and 2018 compiled by Jones et al. (2021) are available from the National Geoscience Data Centre (NGDC) repository (item ID 166966) <https://webapps.bgs.ac.uk/services/ngdc/accessions/index.html?simpleText=landslide%20nepal>. The landslide timing data set, as well as new inventories compiled

for the 2019 monsoon and for western Nepal are available on Zenodo (Burrows et al., 2023). Sentinel-1 data provided by Copernicus and accessed using our Google Earth Engine code for landslide timing (Burrows, 2022). GPM IMERG rainfall data are available from <https://gpm.nasa.gov/data/directory>, APHRODITE from <http://aphrodite.st.hirosaki-u.ac.jp/products.html>. Rain gauge data were provided by the Nepal Department of Hydrology and Meteorology and the Nepal WWF (Not open access), the Global Historical Climatology Network (Menne et al., 2012), and the GFZ PRESSurE project (Andermann et al., 2021) (See Table S1 in Supporting Information S1 for individual gauges). SRTM DEM data are from Farr et al. (2007). Figures were made using PyGMT (Uieda et al., 2023) and Matplotlib (Caswell et al., 2023).

Acknowledgments

This study was supported by funding from the PNTS program (SECURITY project) to OM and KB, and a CNES post-doctoral fellowship to KB.

References

- Amatya, P., Scheep, C., Déprez, A., Malet, J., Slaughter, S., Handwerger, A., et al. (2023). Learnings from rapid response efforts to remotely detect landslides triggered by the August 2021 Nippes earthquake and Tropical Storm Grace in Haiti. *Natural Hazards*. <https://doi.org/10.1007/s11069-023-06096-6>
- Andermann, C., Sitaula, A. P., & Queißer, T. (2021). PRESSurE precipitation time series, Nepal [Dataset]. GFZ Data Services. <https://doi.org/10.5880/GFZ.4.6.2021.002>
- Bell, R., Fort, M., Götz, J., Bernsteiner, H., Andermann, C., Eitzlstorfer, J., et al. (2021). Major geomorphic events and natural hazards during monsoonal precipitation 2018 in the Kali Gandaki Valley, Nepal Himalaya. *Geomorphology*, 372, 107451. <https://doi.org/10.1016/j.geomorph.2020.107451>
- Bogaard, T., & Greco, R. (2018). Invited perspectives: Hydrological perspectives on precipitation intensity-duration thresholds for landslide initiation: Proposing hydro-meteorological thresholds. *Natural Hazards and Earth System Sciences*, 18(1), 31–39. <https://doi.org/10.5194/nhess-18-31-2018>
- Brain, M. J., Moya, S., Kinsey, M. E., Tunstall, N., Petley, D. N., & Sepúlveda, S. A. (2021). Controls on post-seismic landslide behavior in brittle rocks. *Journal of Geophysical Research: Earth Surface*, 126(9), e2021JF006242. <https://doi.org/10.1029/2021jfo06242>
- Burrows, K. (2022). Supplement-to-nhess-2022-21. (software code). <https://doi.org/10.5281/zenodo.6984291>
- Burrows, K., Marc, O., & Andermann, C. (2023). Monsoon triggered landslides in Nepal timed with Sentinel-1 for 2015, 2017, 2018 and 2019 [Dataset]. Zenodo. <https://doi.org/10.5281/zenodo.7970874>
- Burrows, K., Marc, O., & Remy, D. (2022). Using Sentinel-1 radar amplitude time series to constrain the timings of individual landslides: A step towards understanding the controls on monsoon-triggered landsliding. *Natural Hazards and Earth System Sciences*, 22(8), 2637–2653. <https://doi.org/10.5194/nhess-22-2637-2022>
- Caswell, T. A., Lee, A., de Andrade, E. S., Droettboom, M., Hoffmann, T., Klymak, J., et al. (2023). matplotlib/matplotlib: Rel: v3.7.1 [Software]. Zenodo. <https://doi.org/10.5281/zenodo.7697899>
- Collins, B. D., & Jibson, R. W. (2015). *Assessment of existing and potential landslide hazards resulting from the April 25, 2015 Gorkha, Nepal earthquake sequence (Tech. Rep.)*. US Geological Survey.
- Dahal, R. K., & Hasegawa, S. (2008). Representative rainfall thresholds for landslides in the Nepal Himalaya. *Geomorphology*, 100(3–4), 429–443. <https://doi.org/10.1016/j.geomorph.2008.01.014>
- Deijns, A. A., Dewitte, O., Thiery, W., d'Oreye, N., Malet, J.-P., & Kervyn, F. (2022). Timing landslide and flash flood events from SAR satellite: A regionally applicable methodology illustrated in African cloud-covered tropical environments. *Natural Hazards and Earth System Sciences*, 22(11), 3679–3700. <https://doi.org/10.5194/nhess-22-3679-2022>
- Emberson, R., Kirschbaum, D., Amatya, P., Tanyas, H., & Marc, O. (2021). Insights from the topographic characteristics of a large global catalog of rainfall-induced landslide event inventories. In *Natural hazards and Earth system sciences discussions* (pp. 1–33). Copernicus GmbH. <https://doi.org/10.5194/nhess-2021-250>
- Farr, T. G., Rosen, P. A., Caro, E., Crippen, R., Duren, R., Hensley, S., et al. (2007). The shuttle radar topography mission. *Reviews of Geophysics*, 45(2), RG2004. <https://doi.org/10.1029/2005rg000183>
- Ferrario, M. (2019). Landslides triggered by multiple earthquakes: Insights from the 2018 Lombok (Indonesia) events. *Natural Hazards*, 98(2), 575–592. <https://doi.org/10.1007/s11069-019-03718-w>
- Floodlist (2015). Dozens feared dead after floods and landslides in Taplejung, Nepal. Retrieved from <https://floodlist.com/asia/floods-landslides-taplejung-nepal>
- Gabet, E. J., Burbank, D. W., Putkonen, J. K., Pratt-Sitaula, B. A., & Ojha, T. (2004). Rainfall thresholds for landsliding in the Himalayas of Nepal. *Geomorphology*, 63(3–4), 131–143. <https://doi.org/10.1016/j.geomorph.2004.03.011>
- Gautam, D., & Dong, Y. (2018). Multi-hazard vulnerability of structures and lifelines due to the 2015 Gorkha earthquake and 2017 central Nepal flash flood. *Journal of Building Engineering*, 17, 196–201. <https://doi.org/10.1016/j.jobe.2018.02.016>
- Government of Nepal (2017). Nepal Flood 2017: Post-flood recovery needs assessment. Retrieved from <https://un.org.np/resource/nepal-flood-2017-post-flood-recovery-needs-assessment>
- Government of Nepal (2019). Nepal flood, July 2019: 72-hour assessment. Retrieved from <https://reliefweb.int/map/nepal/nepal-flood-july-2019-72-hour-assessment-version-2-30-july-2019>
- Guzzetti, F., Peruccacci, S., Rossi, M., & Stark, C. P. (2008). The rainfall intensity–duration control of shallow landslides and debris flows: An update. *Landslides*, 5(1), 3–17. <https://doi.org/10.1007/s10346-007-0112-1>
- Hibert, C., Michéa, D., Provost, F., Malet, J., & Geertsema, M. (2019). Exploration of continuous seismic recordings with a machine learning approach to document 20 yr of landslide activity in Alaska. *Geophysical Journal International*, 219(2), 1138–1147. <https://doi.org/10.1093/gji/ggz354>
- Huffman, G. J., Bolvin, D. T., Braithwaite, D., Hsu, K., Joyce, R., Xie, P., & Yoo, S.-H. (2015). NASA global precipitation measurement (GPM) integrated multi-satellite retrievals for GPM (IMERG). *Algorithm Theoretical Basis Document (ATBD) Version, 4(26)*.
- Illien, L., Andermann, C., Sens-Schönfelder, C., Cook, K., Baidya, K., Adhikari, L., & Hovius, N. (2021). Subsurface moisture regulates Himalayan groundwater storage and discharge. *AGU Advances*, 2(2), e2021AV000398. <https://doi.org/10.1029/2021av000398>
- Illien, L., Sens-Schönfelder, C., Andermann, C., Marc, O., Cook, K. L., Adhikari, L. B., & Hovius, N. (2022). Seismic velocity recovery in the subsurface: Transient damage and groundwater drainage following the 2015 Gorkha earthquake, Nepal. *Journal of Geophysical Research: Solid Earth*, 127(2), e2021JB023402. <https://doi.org/10.1029/2021jb023402>
- Iverson, R. M. (2000). Landslide triggering by rain infiltration. *Water Resources Research*, 36(7), 1897–1910. <https://doi.org/10.1029/2000wr900090>

- Jones, J. N., Bennett, G. L., Abancó, C., Matera, M. A., & Tan, F. J. (2023). Multi-event assessment of typhoon-triggered landslide susceptibility in the Philippines. *Natural Hazards and Earth System Sciences*, 23(3), 1095–1115. <https://doi.org/10.5194/nhess-23-1095-2023>
- Jones, J. N., Boulton, S. J., Stokes, M., Bennett, G. L., & Whitworth, M. R. (2021). 30-year record of Himalaya mass-wasting reveals landscape perturbations by extreme events. *Nature Communications*, 12(1), 1–15. <https://doi.org/10.1038/s41467-021-26964-8>
- Kinney, M. E., Rosser, N. J., Robinson, T. R., Densmore, A. L., Shrestha, R., Pujara, D. S., et al. (2021). Evolution of coseismic and post-seismic landsliding after the 2015 M_w 7.8 Gorkha earthquake, Nepal. *Journal of Geophysical Research: Earth Surface*, 126(3), e2020JF005803. <https://doi.org/10.1029/2020jf005803>
- Kirschbaum, D., Kapnick, S., Stanley, T., & Pascale, S. (2020). Changes in extreme precipitation and landslides over high mountain Asia. *Geophysical Research Letters*, 47(4), e2019GL085347. <https://doi.org/10.1029/2019gl085347>
- Lambert, L., & Chitrakar, B. (1989). Variation of potential evapotranspiration with elevation in Nepal. *Mountain Research and Development*, 9(2), 145–152. <https://doi.org/10.2307/3673477>
- Larsen, I. J., Montgomery, D. R., & Korup, O. (2010). Landslide erosion controlled by hillslope material. *Nature Geoscience*, 3(4), 247–251. <https://doi.org/10.1038/ngeo776>
- Marc, O., Behling, R., Andermann, C., Turowski, J. M., Illien, L., Roessner, S., & Hovius, N. (2019). Long-term erosion of the Nepal Himalayas by bedrock landsliding: The role of monsoons, earthquakes and giant landslides. *Earth Surface Dynamics*, 7(1), 107–128. <https://doi.org/10.5194/esurf-7-107-2019>
- Marc, O., Hovius, N., Meunier, P., Uchida, T., & Hayashi, S. (2015). Transient changes of landslide rates after earthquakes. *Geology*, 43(10), 883–886. <https://doi.org/10.1130/g36961.1>
- Marc, O., Sens-Schönfelder, C., Illien, L., Meunier, P., Hobiger, M., Sawazaki, K., et al. (2021). Toward using seismic interferometry to quantify landscape mechanical variations after earthquakes. *Bulletin of the Seismological Society of America*, 111(3), 1631–1649. <https://doi.org/10.1785/0120200264>
- Marc, O., Stumpf, A., Malet, J.-P., Gosset, M., Uchida, T., & Chiang, S.-H. (2018). Initial insights from a global database of rainfall-induced landslide inventories: The weak influence of slope and strong influence of total storm rainfall. *Earth Surface Dynamics*, 6(4), 903–922. <https://doi.org/10.5194/esurf-6-903-2018>
- Menne, M. J., Durre, I., Korzeniewski, B., McNeill, S., Thomas, K., Yin, X., et al. (2012). Global historical climatology network - Daily (GHCN-daily), version 3 [Dataset]. National Climatic Data Center. <https://doi.org/10.7289/V5D21VHZ>
- Milledge, D. G., Densmore, A. L., Bellugi, D., Rosser, N. J., Watt, J., Li, G., & Owen, K. J. (2019). Simple rules to minimise exposure to coseismic landslide hazard. *Natural Hazards and Earth System Sciences*, 19(4), 837–856. <https://doi.org/10.5194/nhess-19-837-2019>
- Mondini, A. C., Guzzetti, F., Chang, K.-T., Monserrat, O., Martha, T. R., & Manconi, A. (2021). Landslide failures detection and mapping using Synthetic Aperture Radar: Past, present and future. *Earth-Science Reviews*, 216, 103574. <https://doi.org/10.1016/j.earscirev.2021.103574>
- Owen, L. A., Kamp, U., Khattak, G. A., Harp, E. L., Keefer, D. K., & Bauer, M. A. (2008). Landslides triggered by the 8 October 2005 Kashmir earthquake. *Geomorphology*, 94(1–2), 1–9. <https://doi.org/10.1016/j.geomorph.2007.04.007>
- Petley, D. N., Hearn, G. J., Hart, A., Rosser, N. J., Dunning, S. A., Owen, K., & Mitchell, W. A. (2007). Trends in landslide occurrence in Nepal. *Natural Hazards*, 43(1), 23–44. <https://doi.org/10.1007/s11069-006-9100-3>
- Pradhan, S., Toll, D. G., Rosser, N. J., & Brain, M. J. (2022). An investigation of the combined effect of rainfall and road cut on landsliding. *Engineering Geology*, 307, 106787. <https://doi.org/10.1016/j.enggeo.2022.106787>
- Roback, K., Clark, M. K., West, A. J., Zekkos, D., Li, G., Gallen, S. F., et al. (2018). The size, distribution, and mobility of landslides caused by the 2015 M_w 7.8 Gorkha earthquake, Nepal. *Geomorphology*, 301, 121–138. <https://doi.org/10.1016/j.geomorph.2017.01.030>
- Sharma, S., Khadka, N., Hamal, K., Shrestha, D., Talchabhadel, R., & Chen, Y. (2020). How accurately can satellite products (TMPA and IMERG) detect precipitation patterns, extremities, and drought across the Nepalese Himalaya? *Earth and Space Science*, 7(8), e2020EA001315. <https://doi.org/10.1029/2020ea001315>
- Talchabhadel, R., Shah, S., & Aryal, B. (2022). Evaluation of the spatiotemporal distribution of precipitation using 28 precipitation Indices and 4 IMERG datasets over Nepal. *Remote Sensing*, 14(23), 5954. <https://doi.org/10.3390/rs14235954>
- Uieda, L., Tian, D., Leong, W. J., Schlitzer, W., Grund, M., Jones, M., et al. (2023). PyGMT: A Python interface for the generic mapping tools. Zenodo. (software). <https://doi.org/10.5281/zenodo.772533>
- von Ruette, J., Lehmann, P., & Or, D. (2014). Effects of rainfall spatial variability and intermittency on shallow landslide triggering patterns at a catchment scale. *Water Resources Research*, 50(10), 7780–7799. <https://doi.org/10.1002/2013WR015122>
- Wang, C.-y., & Chia, Y. (2008). Mechanism of water level changes during earthquakes: Near field versus intermediate field. *Geophysical Research Letters*, 35(12), L12402. <https://doi.org/10.1029/2008gl034227>
- Wilson, R. C., & Wieczorek, G. F. (1995). Rainfall thresholds for the initiation of debris flows at La Honda, California. *Environmental and Engineering Geoscience*, 1(1), 11–27. <https://doi.org/10.2113/gseengeosci.1.1.11>
- Wu, W., & Sidle, R. C. (1995). A distributed slope stability model for steep forested basins. *Water Resources Research*, 31(8), 2097–2110. <https://doi.org/10.1029/95WR01136>
- Yatagai, A., Kamiguchi, K., Arakawa, O., Hamada, A., Yasutomi, N., & Kitoh, A. (2012). APHRODITE: Constructing a long-term daily gridded precipitation dataset for Asia based on a dense network of rain gauges. *Bulletin of the American Meteorological Society*, 93(9), 1401–1415. <https://doi.org/10.1175/bams-d-11-00122.1>